

# Systematic *ab initio* study of the phase diagram of epitaxially strained SrTiO<sub>3</sub>

Chien-Hung Lin, Chih-Meng Huang and G. Y. Guo\*

*Department of Physics, National Taiwan University, Taipei, Taiwan 106, Republic of China*

(Dated: July 12, 2021)

We use density-functional theory with the local-density approximation to study the structural and ferroelectric properties of SrTiO<sub>3</sub> under misfit strains. Both the antiferrodistortive (AFD) and ferroelectric (FE) instabilities are considered by calculating all the phases predicted by Pertsev *et al.* [Phys. Rev. B **61**, R 825 (2000)] based on the phenomenological Landau theory. The rotation of the oxygen octahedra and the movement of the atoms are fully relaxed within the constraint of a fixed in-plane lattice constant. We find a rich misfit strain-induced phase transition sequence which is in overall agreement with the prediction by Pertsev *et al.* and is obtained only when the AFD distortion is taken into account. Nevertheless, the calculated locations of the phase boundaries are different from the prediction by Pertsev *et al.* We also find that compressive misfit strains induce ferroelectricity in the tetragonal low temperature phase only whilst tensile strains induce ferroelectricity in the orthorhombic phases only. The calculated FE polarization for both the tetragonal and orthorhombic phases increases monotonically with the magnitude of the strains. The AFD rotation angle of the oxygen octahedra in the tetragonal phase increases dramatically as the misfit strain goes from the tensile to compressive strain region whilst it decreases slightly in the orthorhombic (FO4) phase. This reveals why the polarization in the epitaxially strained SrTiO<sub>3</sub> would be larger when the tensile strain is applied, since the AFD distortion is found to reduce the FE instability and even to completely suppress it in the small strain region. Finally, our analysis of the average polar distortion and the charge density distribution suggests that both the Ti-O and Sr-O layers contribute significantly to the FE polarization.

PACS numbers: 77.22.Ej, 77.84.Dy, 77.80.-e

## I. INTRODUCTION

The strontium titanate (SrTiO<sub>3</sub>, STO) is a prototypical perovskite compound. A mechanically free bulk STO will go through two soft mode-driven phase transitions as the temperature is lowered. First, there is the cubic-to-tetragonal antiferrodistortive (AFD) phase transition at 105 K [1, 2], which results from the phonon induced instability of the *R* point of the Brillouin zone (BZ) boundary and involves the rotation of the TiO<sub>6</sub> octahedra. This is then followed by the ferroelectric (FE) phase transition driven by the instability of the zone-center soft phonon mode. However, the FE transition is not observed in pure STO due to quantum fluctuations [3]. Therefore, it is regarded as an incipient ferroelectric.

In the perovskite ferroelectrics, it is well known both experimentally and theoretically that the polarizations are strongly coupled to strain [4], and thus the properties such as FE transition temperature and polarization magnitude are quite sensitive to external stress. Recently, using techniques such as molecular beam epitaxy and pulsed-laser deposition, it has become possible to grow high-quality perovskite films, and has attracted a great deal of attention. In particular, Haeni *et al.* [5] recently reported a giant shift in FE transition temperature to 293 K for a STO film under biaxial strains. They grew STO films on a (110)-oriented DyScO<sub>3</sub> substrate, corresponding to a biaxial tensile strain of 0.8 %. The results

indicate that even under small strains, a nonpolar STO film can be dramatically transformed to a polar state.

Several theoretical studies have provided insight into the structural properties and temperature dependence of phase transitions in an epitaxial STO film. [6, 7, 8, 9] A phenomenological study of STO thin films under strain by Pertsev *et al.* [6], based on a Landau model fitted to experimental data from bulk phases, predict a rich temperature-strain phase diagram. The effects of in-plane strain and an applied electric field on the dielectric properties of STO epitaxial thin films were calculated by Antons *et al.* [7] using density-functional theory with the local-density approximation (LDA). They find that the polarization can be tuned by the in-plane lattice parameter. Recent *ab initio* calculations by Hashimoto *et al.* [8] confirmed that the ferroelectricity could be induced by applying biaxial strains and also indicated a mechanical origin of the ferroelectricity.

However, in all previous first-principles calculations on the epitaxial STO films, the AFD instability is neglected. This is thought of as an approximation to the high temperature phases. Consequently, many epitaxial strain induced low temperature phases were unable to be investigated in the previous calculations. In this paper, we investigate the effects of the misfit strains on the structure and ferroelectricity in the epitaxially strained STO with both the FE and AFD instabilities taken into account. We use parameter-free first-principles LDA calculations to systematically analyze all the predicted phases by Pertsev *et al.* [6] As a result, we find a rich epitaxial strain induced low temperature phase transition sequence that was unobtainable in the previous *ab initio*

---

\*Electronic address: gyguo@phys.ntu.edu.tw

calculations. We further show the effects of the strains on the AFD instability itself, and hence the difference in the orientation of the oxygen octahedra and also the polarization magnitude compared with the case when the AFD instability is ignored.

The rest of this paper is organised as follows. In Sec. II, we describe the computational technique used and summarize the salient results of the previous phenomenological analysis. In Sec. III, we present and discuss the results of our calculations for the epitaxial STO films under misfit strains. We begin with the determination of the theoretical stable structures of all the possible phases, and then proceed to relate the FE and AFD instabilities to the epitaxial strain and also the underlying electronic band structure. Finally, we give a summary in Sec. IV.

## II. THEORY AND COMPUTATIONAL METHOD

Our *ab initio* calculations for the STO were performed using accurate full-potential projector augmented wave (PAW)[10, 11] method, as implemented in the VASP[12, 13] package. They are based on density-functional theory with the LDA. PAW potentials are used to describe the electron-ion interaction, with the  $4s$ ,  $4p$ ,  $4d$  and  $5s$  states of Sr,  $3d$  and  $4s$  states of Ti, and  $2s$ ,  $2p$  of O being treated as valence states. A conjugate-gradient minimization scheme is used to minimize the Kohn-Sham energy functional, with a plane-wave cut-off energy of 400 eV used throughout. All calculations are performed with a  $6 \times 6 \times 6$  Monkhorst-Pack  $k$ -point mesh. To establish minimum-energy configurations the total forces acting on the atoms are converged to less than 0.01 eV/Å. Our calculations are carried out at the theoretical equilibrium lattice constant of 3.87 Å which is  $\sim 0.9$  % less than the experimental value 3.905 Å, under different strains between 2% and -2%.

### A. Structure optimization

We begin by systematically performing optimizations of the five-atom unit cell of the high-temperature phases (FT1, HT and FO1) and the twenty-atom supercell of all the other possible phases involving the rotations of the oxygen octahedra proposed by Pertsev *et al.*[6] In Fig. 1, we illustrate the supercell which is chosen to describe the AFD instability and give a schematic representation of the atomic displacements for the  $R$  point  $[(111)\pi/a]$  phonon mode. The epitaxial strain on the structural properties of STO is modeled by relaxing either the five-atom or twenty-atom cell of bulk STO under the constrained in-plane lattice constants, differing from the theoretical cubic lattice constant by fractions ranging from -2 % to 2 %. A description of these phases is given in Table I. We have worked out the space groups of all the phases which are also listed in Table I. For each

phase, starting from a structure in which the symmetry is established by appropriately displacing the Ti and O atoms, we relax the atomic positions until the atomic forces fall below a small threshold of 0.01 eV/Å.

Na Sai and Vanderbilt[14] have considered the possible rotations of the oxygen octahedra in the STO but only at zero strain. Here we consider the possible rotations of the oxygen octahedra in the STO under the misfit strains. We focus on the ground state tetragonal phase obtained by freezing in an AFD phonon mode at the  $R$  point of the Brillouin zone (BZ) boundary. This phonon mode corresponds to the rotation of the  $\text{TiO}_6$  octahedra in the opposite directions from one unit cell to the next. For the order parameter  $q_1$ , we take, e.g., the  $x$ -axis as the rotation axis, and adopt a tetragonal supercell with the lattice vectors of length  $\sqrt{2}a$ ,  $\sqrt{2}a$ , and  $c$  along the  $[011]$ ,  $[0\bar{1}1]$ , and  $[200]$  directions, respectively. Similarly, cyclic permutations of the lattice vectors would give rise to the other two rotation axes.

### B. Thermodynamic theory analysis

Pertsev *et al.*[6] used a phenomenological Landau theory to describe the mechanical substrate effect on equilibrium states and phase transitions in epitaxial STO thin films, and developed a misfit strain-temperature phase diagram. Instead of dealing with thin films directly, they computed the structure of the bulk material strained to match a given cubic substrate with square surface symmetry. On the basis of a Landau theory fitted to experimental data from bulk phases, the thermodynamic description may be developed from the power-series expansion of the Helmholtz free-energy density  $F$  in terms of temperature  $T$ , polarization  $\mathbf{P}$  and order-parameter  $\mathbf{q}$ , which corresponds to linear oxygen displacements correlated with the rotation of the oxygen octahedra around one of fourfold symmetry axes, and lattice strain  $S$ , defined as  $S = (a - a_0)/a$  (where  $a$  is the effective lattice constant of the substrate and  $a_0$  denotes the lattice constant of free-stranding cubic cell). By minimizing the free energy  $F(T, S, \mathbf{P}, \mathbf{q})$  with respect to the components of the polarization and structural order parameter, they predicted the equilibrium thermodynamic states of STO films under various temperature-strain conditions. The misfit strain-temperature phase diagram of STO is more complex than  $\text{BaTiO}_3$  (BTO) because the coexistence of two coupled AFD and FE instabilities in this crystal. The results are listed in Table I. Apart from the high temperature tetragonal (HT) phase, they contain purely structural tetragonal and orthorhombic states (ST and SO), purely ferroelectric tetragonal and orthorhombic phases (FT1 and FO1), and four coupled states (FT2, FO2, FO3 and FO4).

In this paper, using parameter-free total-energy methods based on density functional theory, we map out the equilibrium structures of the STO as a function of epitaxial strain at zero temperature, and find out the effect

of misfit strain on the magnitude and orientation of the polarization. The electric polarization is calculated using the Berry phase method[15, 16].

### III. RESULTS AND DISCUSSION

Because of the competition between ferroelectric and structural instabilities, the phases in the STO are more complex than the BTO case[17]. For clearly displaying the calculated energy for each phase as a function of the misfit strain, we separate them into two classes, which are separated by a large energy difference, as shown in Figs. 2 and 5. One contains the high temperature phases, which do not involve the rotation of the oxygen octahedra (FT1, HT, and FO1). The other includes the low temperature phases with the coupling between the polarization and the rotation of the oxygen octahedra.

#### A. High temperature phases

The total energy for each of the three high energy phases as a function of misfit strain is shown in Fig. 2. For large compressive strains, the stable structure is the FT1 phase; for large tensile strains, the FO1 phase is preferred. At the misfit strain of around -0.1 %, there is a continuous transition from the polar FT1 phase to the nonpolar HT phase. As the in-plane misfit strain is increased to 0.3 %, the STO transits from the HT phase to the polar FO1 phase. In Fig. 3, we show the calculated polarizations for the FT1 and FO1 phases versus the misfit strain. The polarization increases dramatically with the magnitude of the misfit strain. For compressive strains larger than -0.1 %, the FT1 phase has the polarization along [001] whilst the FO1 has zero polarization. As the misfit strain gets close to zero, a so-called paraelectric gap within which all the phases exhibit zero polarization, appears (Fig. 3). For tensile strains larger than 0.3 %, the FO1 phase acquires a large polarization along [110], whilst the polarization of the FT1 phase becomes zero.

In Fig. 4, we show the calculated atomic displacements as a function of misfit strain. Under large compressive strains, the atoms in the FT1 phase relax only along the [001] direction. As the in-plane strain decreases, a second-order FT1  $\rightarrow$  HT phase transition follows, and the magnitude of the atomic displacements along [001] gradually diminishes. While the displacements along [001] in the FT1 phase vanish around the zero strain, the displacements in the [110] direction in the FO1 begin to grow as we enter the tensile strain region. With the increasing tensile strain, the displacements in the  $xy$  plane in the FO1 phase continue to grow monotonically. Near zero misfit strain, the atomic displacements change from along the  $z$ -direction to along an  $xy$  plane direction, and the change of the orientation of the polarization follows. From these results, we can see that the in-plane

misfit strain make the polarization to be a monotonically increasing function of the magnitude of the strain, though the polarization direction switches in the paraelectric gap.

The above results are similar to that of the *ab initio* LDA calculations in Ref. 7. Nevertheless, there are some quantitative differences. For example, our estimation of the paraelectric gap (between -0.1 % and +0.3 %) is narrower than that previously obtained (between -0.75 % and +0.54 % in Ref. 7), and this may be attributed to the different potentials used in the present and previous calculations. Furthermore, because the rotations of the oxygen octahedra were not included in the analysis in Ref. 7, the results of Ref. 7 correspond to our results for the high temperature FO1, HT and FT1 phases only.

#### B. Low temperature phases

Due to the interaction between the FE polarization and the AFD structural instability, the low temperature phases are more complex than the high temperature ones. In Fig. 5, we show all the low energy phases predicted in Ref. 6 for the misfit strains between -2 % and 2 %. Roughly speaking, we get nearly the same features as the high temperature case: the presence of two wide misfit strain ranges in which the STO becomes a ferroelectric. This is due to the coupling between the polarization and the misfit strain. In the films grown on the compressive substrates, a FE phase with polarization along the out-of-plane orientation ([001]) appears, while in the case of the tensile substrates, the polarization direction becomes in-plane ([110]). Nevertheless, there are some subtle differences between the high and low temperature cases. First, the structures in the low temperature cases are more stable than in the high temperature ones, because they have a significantly lower total energy (Figs. 2 and 5). Under large compressive strains, the FT2 phase has the lowest energy among the low temperature phases. When the misfit strain is decreased, the STO transits from the polar FT2 phase to the nonpolar ST phase and the two energy curves overlap in a rather wide range of tensile strains (Fig. 5). In contrast, for the high temperature phases, the energy curve of the nonpolar HT phase overlaps with the polar FT1 phase in the tensile strains only, but with the polar FO1 phase in both the tensile and compressive strains. For large tensile strains, the FO4 phase is energetically most favorable. There are some other stable phases occurring only in a small strain region near zero. The energy curves of the FO2 and SO are almost the same, and their trends are also similar to the FO4 phase in the small strain region, but split off from the FO4 with increasing tensile strain (Fig. 5). Similarly, the curve of the FO3 phase lies on the ST phase one in the compressive strain but splits off from it when grown on the tensile substrate. As the compressive or tensile strain increases, the structural symmetry is broken, thereby splitting the energy degeneracy. However, in the small strain region,

the total energies for many different phases are almost in overlap with each other. Nevertheless, accurate distinction between different stable phases can be achieved by calculating the second derivative of the total energy with respect to the strain. The strain divisions obtained this way, between FT2 and ST, ST and FO3, FO3 and FO2, FO2 and FO4 are -0.558 %, -0.221 %, 0.197 %, and 0.442 %, respectively. Remarkably, this rich low temperature phase-versus-strain sequence is generally consistent with the prediction of the phenomenological theory by Pertsev *et al.*[6] The main difference is the precise location of the low temperature phase boundaries. In particular, we predict that the FO3 phase is located in the strain region between -0.22 % and 0.20 % whilst it falls in the strain region from around -0.023 % to -0.005 % according to Pertsev *et al.*[6] The FO2 is predicted to stride the zero strain in Ref. 6, instead of the FO3 phase. Since the FO2 and FO3 phases have different polarization directions and also different order parameter  $\mathbf{q}$ , this difference can perhaps be easily examined by further experiments. Of course, our calculations are for the zero and very low temperatures only. Consequently, we cannot discuss the temperature effect on the epitaxial STO structures which may lift the energy degeneracy, and hence the misfit strain-temperature phase diagram.

In Fig. 6, we show the calculated polarization (including both ionic and electronic contributions) of the FT2, FO2, FO3 and FO4 phases as a function of misfit strain. Interestingly, the energy curves of all the low temperature phases converge to the same energy at the zero strain (Fig. 5). However, away from this narrow window near the zero strain, the lowest energy phase is the FT2 under the large compressive strains and the FO4 in the tensile strain region (Fig. 5). Therefore, we concentrate on these two phases only below. The results are similar to the high-temperature phase one. The polarization is along [001] and [110] for the compressive and tensile strains, respectively. It exhibits a monotonic increase with the magnitude of the misfit strain. There is also a paraelectric gap centered at the zero strain, now between -0.4 % and 0.4 %. This gap is larger than the high temperature one. Nevertheless, the size of this gap should be the upper bound because we have not considered the other FE phases in the paraelectric region. The polarization for the FO2 and FO3 phases becomes zero when the misfit strain drops below 0.2 % and 0.3 %, respectively. Therefore, the overall paraelectric gap for the low temperature phases is between -0.4 % and 0.2 %. Interestingly, a comparison of the polarization-versus-strain curves for the FT1 phase in Fig. 3 and the FT2 phase in Fig. 6 reveals that the AFD instability reduces the polarization in the large compressive strain region, and completely suppresses it in the small strain region, thus enlarging the paraelectric gap. Note that the atomic structures of the FT1 and FT2 phases are almost the same except that the FT2 phase can accommodate the AFD rotations of the oxygen octahedra whilst the FT1 phase cannot. Indeed, the AFD distortion as char-

acterized by the rotation angle of the oxygen octahedra in the FT2 is strong in the compressive strain region, as shown in Fig. 8 below.

We now further quantify the strength of the FE and AFD distortions. In the FE case, let us define the average polar distortion along the  $i$ -direction,  $p_i$ , in the  $1 \times 1$  unit cell of each atomic layer. For the  $\text{TiO}_2$  layers,

$$p_i = \Delta_i(\text{Ti}) - \frac{\Delta_i(\text{O}_1) + \Delta_i(\text{O}_2)}{2},$$

and for the SrO layers,

$$p_i = \frac{\Delta_i(\text{Sr}_1) + \Delta_i(\text{Sr}_2)}{2} - \Delta_i(\text{O}),$$

where  $\Delta_i$  are the atomic displacements in the  $i$ -direction relative to the undistorted symmetric  $1 \times 1$  perovskite structure. The computed results describing the strength of the FE distortion in each atomic layer are plotted in Fig. 7. Note that for the ST and SO phases, the average polar distortion is zero for all the strains, and therefore, is not shown in Fig. 7.

It is clear from Fig. 7 that in the compressive strain region, the average polar distortion in the FT2 phase is larger in the  $\text{TiO}_2$  layers than in the SrO layers. Interestingly, in the FO4 phase, it is the opposite, i.e., the average distortion in the tensile strain region is larger in the SrO layer than in the  $\text{TiO}_2$  layer. Around the zero strain, the average distortion is significant only in the  $\text{TiO}_2$  layer in the FO3 and FO2 phases. This indicates that in the vicinity of the zero strain, only the FO2 and FO3 phases have a significant polarization, thereby giving a microscopic explanation to the results of the previous thermodynamical analysis[6] (Table I). Note also that the average polar distortion along the in-plane direction in the tensile strain region in the FO3 and FO4 phases is larger than along the z-direction in the compressive strain region in the FT2 phase. This suggests that the ionic contribution to the polarization in the FO4 phase in the tensile strain region would be larger than in the FT2 phase in the compressive strain region, and explains the calculated polarizations displayed in Fig. 6.

The strength of the AFD distortion is characterized by the  $\text{TiO}_4$  rotation angle  $\theta$ , in each  $\text{TiO}_2$  layer. In Fig. 8, we present the calculated rotation angle of the oxygen octahedra as a function of misfit strain for the low-temperature phases due to the AFD instability. The calculated tilting angle of the oxygen octahedra at zero strain ( $6^\circ$ ) is overestimated in our calculations, as also in Ref. 14, compared to the experimental value of  $2^\circ$ [18]. This discrepancy between the *ab initio* calculations and the experiments may be caused by the LDA error or by the quantum fluctuations [19] which should reduce the rotations of the oxygen octahedra, or by both. The results nonetheless provide us some qualitative insight into how oxygen octahedra rotate under the applied strains. Fig. 5 shows that under compressive strains, the FT2, ST and FO3 are the low energy phases and the rotation angle of the  $\text{TiO}_6$  octahedra along [001] increases with

the magnitude of the misfit strain. In contrast, under the tensile strains, the FO4, FO2 and SO become the low energy phases (Fig. 5) and the rotation axis changes to lie in the  $xy$  plane. In the FO2 and SO phases, the rotation angle of the  $\text{TiO}_6$  octahedra again increases with the magnitude of misfit strain (Fig. 8). Interestingly, the rotation of the oxygen octahedra in the FO4 phase is nearly independent of applied strain (Fig. 8). Note that there are two equivalent rotation axes along  $[100]$  and  $[010]$ , respectively, for the FO4 phase. Therefore the linear displacements of the oxygen atoms due to the rotations and the rotation angles are equal for the two axes. In Fig. 8, we thus show only the rotation angle for either  $[100]$  or  $[010]$ . Interestingly, Figs. 6 and 7 show that the FE instability as manifested in the electric polarization and the average polar distortion, in both the FT2 phase in the large compressive strain region and the FO4 phase in the large tensile strain one, grow as the magnitude of the strains is increased, though it is stronger in the FO4 phase than in the FT2 phase. In contrast, the behavior of the AFD instability as manifested in the rotation of the oxygen octahedra, is different. Fig. 8 shows that the tilting angle of the oxygen octahedra in the FT2 (also ST and FO3) phase increases dramatically as the misfit strain goes from the strong tensile region through zero strain to the strong compressive region, while it remains nearly as a relatively small constant for the FO4 phase. This explains why the calculated polarization is larger for the FO4 phase under the tensile strain than the FT2 phase when the AFD instability which tends to suppress the FE instability, is taken into account.

### C. Charge density and polarization

In order to better understand the chemical bonding and also the origin of the electric polarization in the strain induced FE phases, we examine the calculated charge density distributions. Figure 9 shows the contour plots of the charge density differences between calculated charge densities and those obtained by a superposition of the free atomic charge densities for the FT2 phase under compressive strain of -1.6 % and the FO4 phase at tensile strain of 1.6 %. It can be seen from the calculated charge density difference distribution on the (001) SrO planes in Fig. 9 that in the both structures, the charge is depleted in the inner region of the Sr sites, whilst, in contrast, there is considerable charge buildup on the O sites and also in the outer region of the Sr sites. This indicates that the Sr-O bonding is predominantly ionic. The ionic Sr-O bonding can be further seen from the fact that the charge distribution at the Sr sites are nearly spherical. This is because the Sr 5s valence electrons have moved to the neighboring O atoms which have high electron affinity, with the spherical symmetry ionic cores left behind. On the other hand, the bonding between the Ti and O atoms are strongly covalent, as can be seen from the calculated charge density difference distributions on the (001) and

(100) TiO planes in Fig. 9. There is pronounced charge buildup in the vicinity of the Ti-O bond center whilst there is significant charge depletion on both the Ti and O sites.

Figure 9 also shows that the charge density distribution on both the (001) SrO and TiO planes in the FT2 phase has a fourfold symmetry at the O and Ti sites, respectively. As a result, there is no electric polarization in the  $x-y$  plane. In contrast, on the (001) TiO plane in the FO4 phase [Fig. 9(d)] the charge buildup is much stronger in the central region of the two right Ti-O bonds than in the left two ones, and it leans towards the vertical down direction in all the four Ti-O bond regions, thus resulting in an electric polarization along the  $[110]$  direction (vertical up direction). Clearly, the charge density distribution on the (001) SrO plane in the FO4 phase also lean downwards, suggesting that the SrO layers also contribute to the polarization, being in conflict with common wisdom. On the (100) TiO planes [Fig. 9(e-f)], the strong charge buildup in the FT2 phase clearly lean downwards and is symmetric with respect to the vertical line through the center O atom in the FT2 phase, whilst, in contrast, it leans towards left and is symmetric with respect to the horizontal line through the center O site in the FO4 phase. As a result, the FT2 phase has a polarization along  $[001]$  whilst the FO4 phase exhibit a polarization along  $[110]$ .

## IV. SUMMARY

In this paper, we have performed *ab initio* LDA calculations for the STO under various misfit strains. A unique part of this work is that we have considered both the high-temperature and low-temperature phases of the STO proposed by Pertsev *et al.*[6] such that both the AFD and FE structural instabilities have been investigated, unlike previous *ab initio* studies in which the AFD rotations of the oxygen octahedra have been neglected. As a result, we find a rich misfit strain-induced low temperature phase transition sequence which is in overall agreement with the prediction by Pertsev *et al.* Nevertheless, the calculated locations of the phase boundaries are rather different from the prediction by Pertsev *et al.* In particular, we predict that the FO3 phase is located in the strain region between -0.22 % and 0.20 % whilst the FO2 would stride the zero strain according to Pertsev *et al.* Since the FO2 and FO3 phases have different polarization directions and also different order parameter  $\mathbf{q}$ , this difference can perhaps be easily examined by the future experiments. By analyzing the FE atomic displacements and the AFD rotations of the oxygen octahedra, we provide a comprehensive microscopic insight into the effects of both the FE and AFD instabilities on the ferroelectric properties of STO under the epitaxial strains. We also find that at low temperatures, compressive strains would induce FE polarization in the FT2 phase only whilst tensile strains induce po-

larization in the orthorhombic phases only. The calculated ferroelectric polarization for both the FE tetragonal and orthorhombic phases increases monotonically with the magnitude of the strains, with the polarization in the tensile strain region being larger than in the compressive region. The AFD rotation angle of the oxygen octahedra in the FT2 phase increases dramatically as the misfit strain goes from the tensile to compressive strain region whilst it remains nearly unchanged in the FO4 phase. This reveals why the polarization in the epitaxially strained STO would be larger when the tensile strain is applied, since we find that the AFD distortion would reduce the FE instability and even completely suppress it in the small strain region. Finally, by analysing the so-

called average polar FE distortion and the charge density distribution, we find that both the Ti-O and Sr-O layers contribute significantly to the FE polarization.

### Acknowledgments

The authors gratefully acknowledge financial supports from National Science Council of the Republic of China. They also thank National Center for High-performance Computing of the Republic of China for providing CPU time.

- 
- [1] G. Shirane and Y. Yamada, Phys. Rev. **177**, 858 (1969)
  - [2] H. Thomas and K. A. Müller, Phys. Rev. Lett. **21**, 1256 (1968)
  - [3] K. A. Müller and H. Burkard, Phys. Rev. B **19**, 3593 (1979)
  - [4] H. Uwe and T. Sakudo, Phys. Rev. B **13**, 271 (1976)
  - [5] J. H. Haeni, P. Irvin, W. Chang, R. Uecker, P. Reiche, Y. L. Li, S. Choudhury, W. Tian, M. E. Hawley, B. Craigo, A. K. Tagantsev, X. Q. Pan, S. K. Streiffer, L. Q. Chen, S. W. Kirchoefer, J. Levy and D. G. Schlom, Nature **430**, 758 (2004)
  - [6] N. A. Pertsev, A. K. Tagantsev and N. Setter, Phys. Rev. B **61**, R825 (2000); *ibid.* **65**, 219901 (E) (2002)
  - [7] A. Antons, J. B. Neaton, K. M. Rabe and D. Vanderbilt, Phys. Rev. B **71**, 024102 (2005)
  - [8] T. Hashimoto, T. Nishimatsu, H. Mizuseki, Y. Kawazoe, A. Sasaki and Y. Ikeda, Jpn. J. Appl. Phys. **44**, 7134 (2005).
  - [9] O. Diéguez, K. M. Rabe, and D. Vanderbilt, Phys. Rev. B **72**, 144101 (2005).
  - [10] P. E. Blöchl, Phys. Rev. B **50**, 17953 (1994)
  - [11] G. Kresse and D. Joubert, Phys. Rev. B **59**, 1758 (1999)
  - [12] G. Kresse and J. Hafner, Phys. Rev. B **47**, 558 (1993)
  - [13] G. Kresse and J. Furthmüller, Comput. Mater. Sci. **6**, 15 (1996)
  - [14] Na Sai and D. Vanderbilt, Phys. Rev. B **62**, 13942 (2000)
  - [15] R. D. King-Smith and D. Vanderbilt, Phys. Rev. B **47**, 1651 (1993)
  - [16] R. Resta, Ferroelectrics **136**, 51 (1992)
  - [17] O. Diéguez, S. Tinte, A. Antons, C. Bungaro, J. B. Neaton, K. M. Rabe and D. Vanderbilt, Phys. Rev. B **69**, 212101 (2004)
  - [18] E. Courtens, Phys. Rev. Lett. **29**, 1380 (1972)
  - [19] W. Zhong and D. Vanderbilt, Phys. Rev. B **53**, 5047 (1996)
  - [20] S. Piskunov, E. Heifets, R. I. Eglitis, and G. Borstel, Comput. Mater. Sci. **29**, 165 (2004)

### Figure captions

Fig. 1 (Color online) A [001] projected section of the SrTiO<sub>3</sub> lattice illustrating the linear displacements of the oxygen ions associated with an antiferrodistortive phonon mode at the  $R$  point  $[(111)\pi/a]$  of the Brillouin zone boundary (upper panel). The thick square frame indicates the supercell used in our calculations. The lower panel is a schematic representation of the rotations of the oxygen octahedra in the soft phonon-mode.

Fig. 2 (Color online) Calculated total energy of the high temperature epitaxial SrTiO<sub>3</sub> phases versus misfit strain (see Table I for the symbols of the phases). The vertical dotted lines denote the boundaries between the paraelectric and ferroelectric phases (see Fig. 3).

Fig. 3 Calculated polarization of the FT1 and FO1 phases versus misfit strain. The polarizations for the FT1 and FO1 phases are along [001] and [110], respectively. The vertical dotted lines denote the boundaries between the paraelectric and ferroelectric phases.

Fig. 4 (Color online) Calculated atomic displacements  $\Delta$  in the FT1 phase (compressive strains only) and the FO1 phase (tensile strains only). The subscripts label the directions of the displacements.

Fig. 5 (Color online) Calculated total energy of the low temperature epitaxial SrTiO<sub>3</sub> phases versus misfit strain. The vertical dotted lines denote the boundaries between the paraelectric and ferroelectric phases (see Fig. 6).

Fig. 6 (Color online) Calculated polarization of the FT2, FO2, FO3 and FO4 phases versus different strain. The polarization for the FT2 phase is along [001]; the polarization for the FO3 and FO4 phases is along [110]; the polarization for the FO2 phase is along [100]. The vertical dotted lines denote the boundaries between the

TABLE I: The epitaxial SrTiO<sub>3</sub> phases predicted by Pertsev *et al.* [6] Nonzero components of the polarization  $\mathbf{P}$  and the order parameter  $\mathbf{q}$  are the characteristics of the different phases in the epitaxial SrTiO<sub>3</sub> films grown on the cubic substrates. Phases are labeled by the lattice symmetry (T = tetragonal, O = orthorhombic) and also the type of the instability (S = structural, F = ferroelectric, H = high temperature). Also listed are the space groups ( $G_s$ ) for all the phases found in the present work.

Phase	HT	ST	SO	FT1	FT2	FO1	FO2	FO3	FO4
$\mathbf{P}$				$P_3$	$P_3$	$ P_1  =  P_2 $	$P_1$ (or $P_2$ )	$ P_1  =  P_2 $	$ P_1  =  P_2 $
$\mathbf{q}$		$q_3$	$q_1$ (or $q_2$ )		$q_3$		$q_2$ (or $q_1$ )	$q_3$	$ q_1  =  q_2 $
$G_s$	P4/mmm	I4/mcm	Fmmm	P4mm	I4cm	Amm2	Fmm2	Ima2	Ima2

paraelectric and ferroelectric phases.

Fig. 7 (Color online) The average layer ferroelectric polar distortion (see text),  $p_i$ , versus misfit strain, in percentage of the lattice parameter. Solid and dashed curves denote the distortions in the TiO<sub>2</sub> and SrO layers, respectively. The subscripts label the directions of the distortions. Note that for the ST and SO phases, the average polar distortion is zero for all the strains.

Fig. 8 (Color online) Calculated rotation angle of the oxygen octahedra for all the low temperature epitaxial SrTiO<sub>3</sub> phases versus misfit strain.

Fig. 9 (Color online) Contour plots of the charge density differences between the calculated charge densities and those obtained by a superposition of the free atomic charge densities in different projected planes for the FT2 phase under compressive strain of -1.6 % and the FO4 phase at tensile strain of 1.6 %. (a) and (b) are for the (001) SrO<sub>2</sub> planes. (c) and (d) are for the (001) TiO planes. (e) and (f) are for the (100) TiO planes. The dark (blue) curves denote the positive contour levels with contour step of 0.025 e/Å<sup>3</sup> and the light (red) dashed curves denote the negative ones with contour step of 0.084 e/Å<sup>3</sup>.

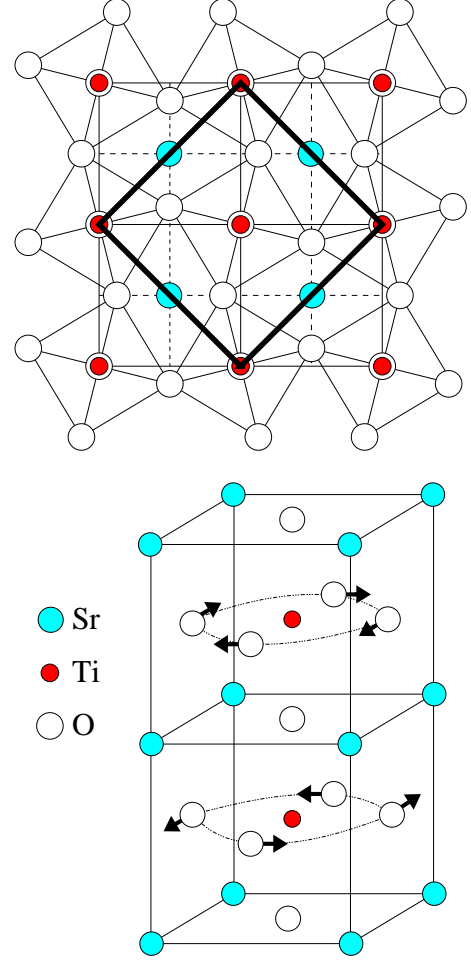


FIG. 1:

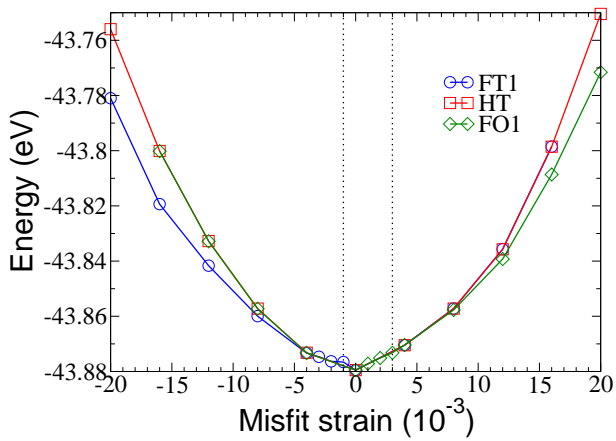


FIG. 2:

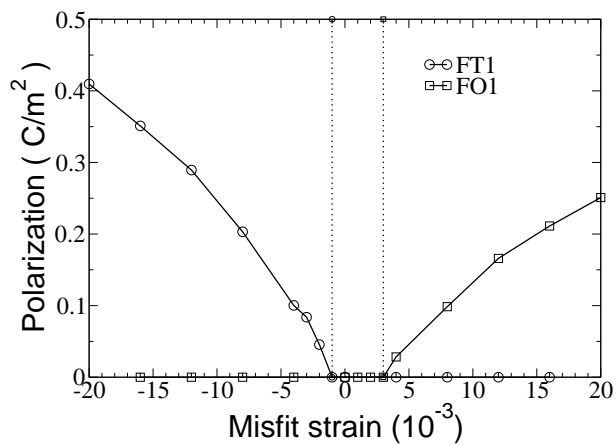


FIG. 3:

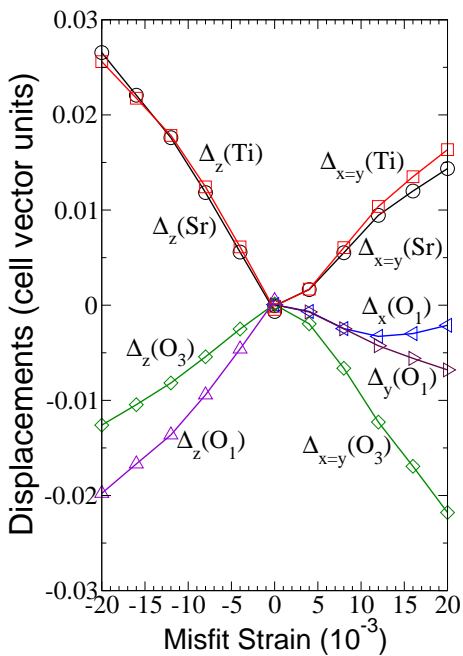


FIG. 4:



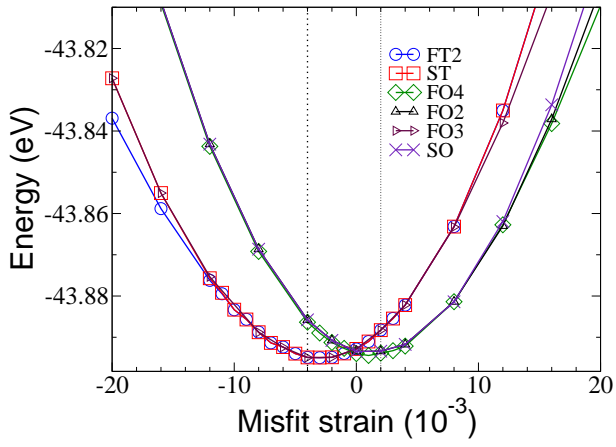


FIG. 5:

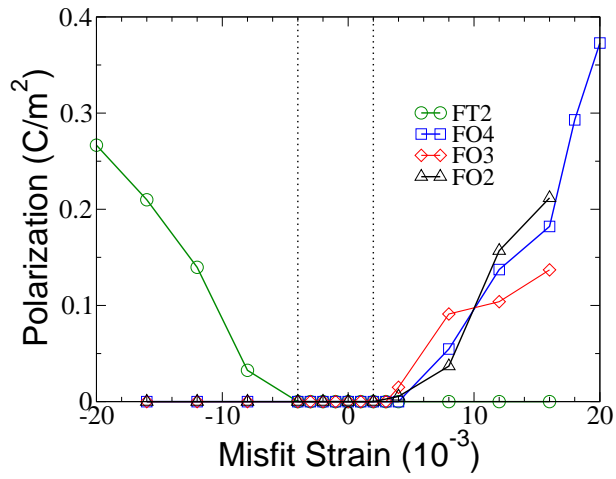


FIG. 6:

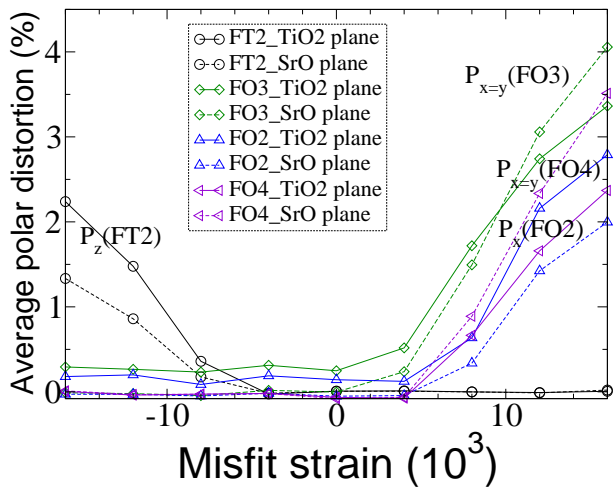


FIG. 7:

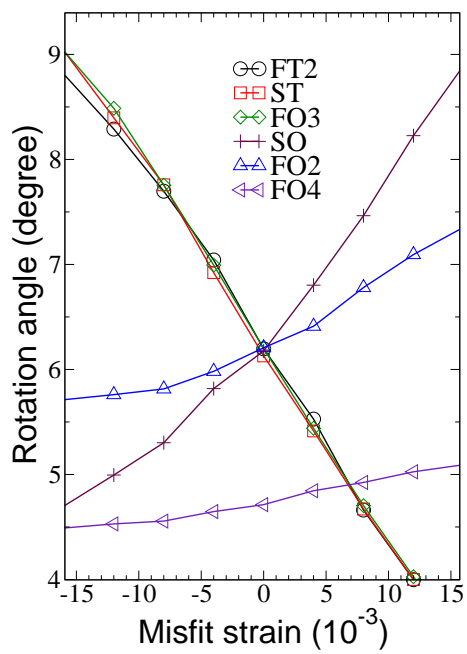


FIG. 8:

FIG. 9: